



On the scaling and critical layer in a turbulent boundary layer over a compliant surface

Yuhui Lu¹, Tianrui Xiang¹, Tamer A. Zaki¹ and Joseph Katz^{1,†}

¹Department of Mechanical Engineering, Johns Hopkins University, Baltimore, MD 21218, USA

(Received 2 September 2023; revised 9 November 2023; accepted 27 December 2023)

Simultaneous time-resolved measurements of wall deformation and the 3-D velocity field in boundary layers over a compliant surface are performed by integrating Mach Zehnder interferometry with tomographic particle tracking velocimetry. The pressure is calculated by spatially integrating the material acceleration. Combining data obtained from several references, trends of the deformation r.m.s. scaled by the compliant wall thickness collapse when plotted vs pressure fluctuations scaled by the material shear modulus. For the present data, at all Reynolds numbers, the deformation waves travel at 53% of the free-stream velocity and have a preferred wavelength of three times the thickness. The latter is consistent with theoretical models. Adopting insight derived from atmospheric wind–wave interactions, the pressure–deformation correlations peak at or slightly above the ‘critical layer’, where the mean flow speed is equal to the surface wave speed. This layer is located within the log layer, and when expressed using inner variables, increases in elevation with increasing Reynolds number. For the entire region below the critical layer, wavenumber–frequency spectra of pressure and vertical velocity fluctuations indicate that the turbulence is phase locked and travels with the deformation, even for deformation amplitudes much smaller than a wall unit. In contrast, above the critical layer, the turbulence is advected at the local mean streamwise velocity, and its correlation with the deformation decays rapidly. These findings indicate that the height of the zone dominated by flow–deformation interactions is determined by the surface wave speed, and its variations are caused by deformation-induced modifications to the mean velocity profile.

Key words: boundary layers

1. Introduction

As summarized in reviews (Gad-el Hak 1986*a*; Carpenter, Davies & Lucey 2000), the interactions between compliant surfaces and boundary layers have been investigated

† Email address for correspondence: katz@jhu.edu

extensively since the bio-inspired attempts to reduce skin friction by Kramer (1960). Linear theoretical models predicting the response of viscoelastic coatings to uniform harmonic excitation by pressure and shear stress based on solutions to the Helmholtz equation have been discussed in Chase (1991) and Benschop *et al.* (2019). They predict that the wavelength of peak wall response is three times the wall thickness, and that the pressure is the dominant contributor to the deformation. While early numerical simulations model the wall using springs and dampers (e.g. Kim & Choi 2014), recent direct numerical simulations (DNS) already compute the flow in the boundary layer and within the compliant wall (Rosti & Brandt 2017; Esteghamatian, Katz & Zaki 2022). Experimental velocity profiles in the inner part of the boundary layers and the wall deformation are available in Zhang *et al.* (2017), Wang, Koley & Katz (2020) and Greidanus *et al.* (2022). While trends vary, these DNS and experiments show a decrease in the velocity in the buffer and viscous sublayers that increases in severity with the deformation amplitude relative to the wall unit, $\delta_v = \nu/u_\tau$, where ν is the kinematic viscosity and $u_\tau = (\tau_w/\rho)^{1/2}$, with τ_w and ρ being the wall shear stress and fluid density, respectively. Wang *et al.* (2020) and Greidanus *et al.* (2022) observe deviations in the inner-layer profiles even for deformation amplitudes, d , much smaller than δ_v ($d^+ = d/\delta_v \ll 1$). The extent of influence on the magnitude and slope of the log layer profiles differs among these studies.

The present analysis of recently obtained experimental data highlights the importance of a ‘critical layer’ introduced by Miles (1957) for characterizing wind–wave interactions in oceanography. At the critical height, $y = y_c$, the mean streamwise velocity, $U(y)$, is equal to the surface wave speed, U_{sw} . Lighthill (1962) demonstrates that the energy transfer from the wind to the wave is concentrated at the critical layer, but since it is separated from the wave, the interaction occurs at all $y < y_c$. Numerous studies, e.g. Young & Wolfe (2014) and Carpenter, Guha & Heifetz (2017), have since attempted to model this energy transfer, and the latter has been validated recently by Carpenter, Buckley & Veron (2022) using experimental data. In this paper, we demonstrate the important role that the critical layer plays in interactions between a compliant wall and a turbulent boundary layer.

The present experiments involve simultaneous measurements of the time-resolved three-dimensional (3-D) velocity and pressure fields as well as the two-dimensional (2-D) distribution of surface deformation. Data are obtained at three friction Reynolds numbers ($Re_\tau = u_\tau \delta/\nu$, where δ is the boundary-layer thickness), hence there are different deformation magnitudes relative to the boundary-layer length scales. Combining data from several references, we show that trends of the deformation r.m.s. scaled by the compliant wall thickness collapse and are nearly linear when plotted vs pressure fluctuations scaled by the shear modulus. The pressure–deformation correlation peaks at or slightly above y_c , which is located in the log layer. At lower elevations, wavenumber–frequency spectra of pressure and vertical velocity fluctuations indicate that the turbulence is phase locked and travels with the deformation, even for $d^+ \ll 1$. In contrast, at $y > y_c$, the turbulence is advected at the local mean streamwise velocity, and its correlation with the deformation decays rapidly. These trends differ fundamentally from those of smooth wall boundary layers. The outline of the paper is as follows: § 2 presents the experimental set-up and data processing procedures, results are discussed in § 3 and conclusions are summarized in § 4.

2. Experimental set-up and measurement procedures

The present measurements are performed in a recently constructed refractive-index-matched water tunnel, which uses the same inlet diffuser, settling chamber, test section and diffuser as those described in Wang *et al.* (2020). However, additional screens are

added to the settling chamber to reduce the free-stream turbulence. Recent Particle Image Velocimetry (PIV) measurements show that the r.m.s. of free-stream velocity fluctuations is less than 0.7%. The fluid is a 62% by weight aqueous NaI solution that has the same refractive index (1.487) as acrylic. The bottom acrylic window of the $20 \times 15 \text{ cm}^2$ cross-section and 85 cm long test section is coated with a 5 mm thick transparent compliant material made of PDMS (Dow Corning Sylgard[®]184 Polydimethylsiloxane) mixed with a silicone softener (Sylgard[®]527) at a ratio of 1:7.5 to obtain a storage modulus, E , of 158 kPa and loss tangent of 0.01 (Wang *et al.* 2020). For the present tests, we have made a fresh compliant wall, following the Wang *et al.* (2020) recipe, including the same specific brand of PDMS and softener and the same manufacturing procedures, namely mixing ratio, curing temperature, curing time, ambient pressure, etc. We have also verified that the storage modulus and loss modulus remain unchanged, at least at low frequencies ($<20 \text{ Hz}$) based on tests performed using Texas Instrument Q850[®] dynamic mechanical analyzer. The different refractive index of the coating (1.406) is needed for measuring the wall deformation using interferometry. The boundary layer is tripped, 48 cm upstream of the measurement region, with a series of 0.5 mm high grooves to establish an equilibrium turbulent boundary layer, as confirmed by the profiles of free-stream velocity and Reynolds stresses for a smooth rigid-wall boundary layer (Wang *et al.* 2020). The flow and compliant wall deformation are measured at three Re_τ , ranging from 3300 to 8900, or $E/(\rho U_0^2)$ ranging from 2.5 to 20.3. The values of δ and U_0 , the mean velocity outside of the boundary layer, are determined from large field-of-view stereo PIV measurements, and δ_v is estimated from a fit to the velocity profiles in the log layer using tomographic particle tracking velocimetry (TPTV) data. In the following discussions, (x, y, z) and (u, v, w) are the streamwise, wall-normal and spanwise directions and velocity components, respectively, with U_i and u'_i referring to ensemble averaged and fluctuating quantities.

Simultaneous measurements of the time-resolved volumetric flow field and spatial distribution of wall deformation are performed using an integrated system involving TPTV for measuring the flow, and Mach Zehnder interferometry (MZI) for mapping the surface deformation. The system is illustrated in figure 1(a), dimensions are listed in table 1, and descriptions of components can be found in Zhang *et al.* (2015). For TPTV, the flow field is illuminated by a 10 mm thick laser sheet (Photonics DM60-527 ND:YLF laser) at frequencies varying between 4.5 and 8.7 kHz. The liquid is seeded with 13 μm diameter silver-coated hollow glass spheres that have a specific gravity of 1.6, slightly lighter than the liquid (1850 kg m^{-3}). The images are recorded by four high-speed cameras (PCO Dimax S4), marked as Cam 1–4, located on both sides of the test section. Mirrors M1 and M2 are backside polished and have a reflectivity of 99.9%. They are used as beam splitters, with the latter reflecting the light to the test section to enhance the illumination intensity. The remaining 0.1% is transmitted through M1 and M2 to create the reference and object beams of the interferometer, respectively, and their pathlengths are matched with mirrors M4–M7. As light propagates through the compliant surface, its phase is modulated by the wall deformation, and the resulting interference pattern is recorded by a fifth high-speed camera (Phantom V2640), which is marked as Cam 5. For each Re_τ , data are recorded for $\sim 3 \text{ s}$, resulting in 13 000–26 000 frames. Specific values are provided in table 1.

For flow and pressure measurements, the 3-D particle tracks are detected using the ‘Shake-The-Box’ Lagrangian tracking method based on the Lavision Davis[®] 10.2 software. Coarse calibration performed translating a target, followed by a self-calibration, give a mean tomographic disparity of 0.05 pixel and a standard deviation of 0.14 pixel. The vertical resolution is $29.6 \mu\text{m pixel}^{-1}$, corresponding to $2.2\delta_v$ at the lowest Re_τ , and

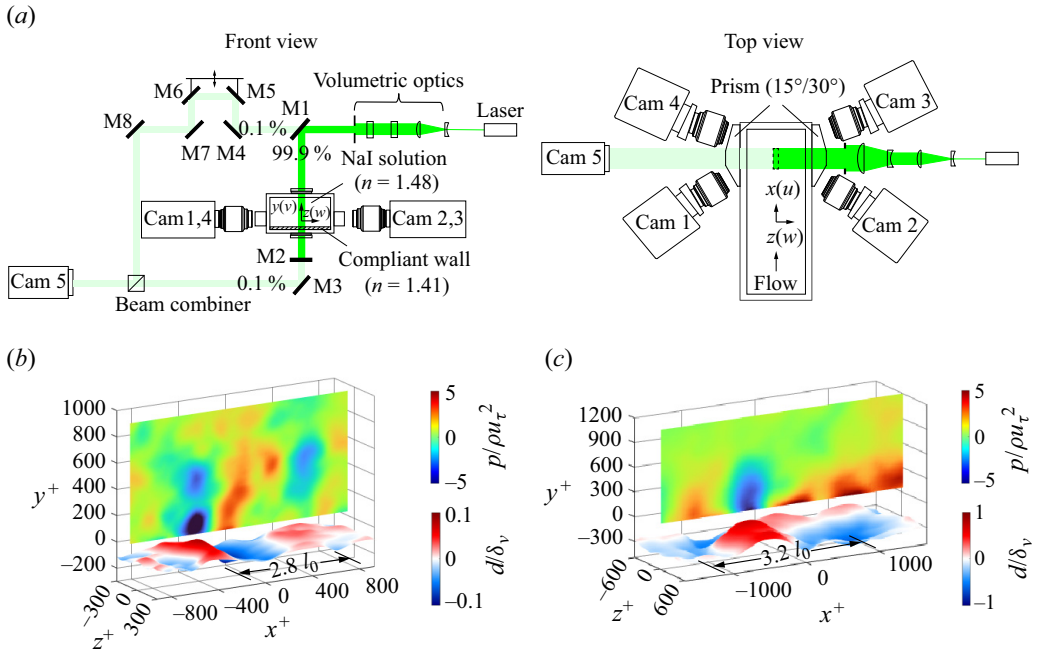


Figure 1. (a) The integrated MZI and TPTV set-up for simultaneous time-resolved measurements of the 2-D distribution of compliant wall deformation and the 3-D flow field (Zhang, Miorini & Katz 2015). Sample instantaneous snapshots of wall deformation (in exaggerated scales) and pressure in the spanwise plane of maximum deformation at (b) $Re_\tau = 3300$ and (c) $Re_\tau = 6700$.

Re_τ (from log fit)	3300	6700	8900
$E/\rho U^2$	20.3	4.5	2.5
d_{peak}^+	0.22	1.28	3.46
d_{rms}^+	0.03	0.17	0.44
y_c^+ and (y_c/δ)	63 (0.019)	165 (0.025)	193 (0.022)
TPTV sample volume	$27 \times 12.8 \times 8.2 \text{ mm}^3$	$23 \times 8.3 \times 8.2 \text{ mm}^3$	$23 \times 5.5 \times 8.2 \text{ mm}^3$
$x \times y \times z$ in mm, (δ_v)	$(2000 \times 950 \times 610 \delta_v^3)$	$(3370 \times 1220 \times 1200 \delta_v^3)$	$(4540 \times 1090 \times 1620 \delta_v^3)$
camera field of view {pixels}	{1104 × 500}	{1008 × 332}	{1008 × 240}
Interpolated TPTV vector spacing in mm, (δ_v)	0.4 mm (29.6 δ_v)	0.4 mm (58.6 δ_v)	0.4 mm (78.9 δ_v)
MZI field of view $x \times z$ in mm and (pixels)	$27 \times 10 \text{ mm}^2$ (2000 × 822)	$27 \times 10 \text{ mm}^2$ (2000 × 822)	$27 \times 10 \text{ mm}^2$ (2000 × 822)
Spatial resolution of wall deformation in mm, (δ_v)	0.2 mm (15 δ_v)	0.2 mm (29.6 δ_v)	0.2 mm (39.9 δ_v)
Frame rate	4545 Hz	6452 Hz	8696 Hz
Record length in s, (no. of frames)	2.84 s (12 909)	2.94 s (18 992)	3.02 s (26 270)

Table 1. Experimental conditions.

$5.8\delta_v$ at the highest Re_τ . Following Agarwal *et al.* (2021), the unstructured velocity and material acceleration are obtained based on polynomial fit to the particle tracks. The data are then interpolated onto a structured grid (see table 1 for spacing) using a constrained cost minimization (CCM) method, which minimizes differences from the experimental data and the previous iteration, and forces the velocity to be divergence-free, and the material acceleration curl-free away from the wall, while accounting for the viscous terms in the buffer and viscous sublayers, i.e. $\nabla \times ((D\mathbf{u}/Dt) - \nu \nabla^2 \mathbf{u}) = 0$. The 3-D pressure distribution is calculated by spatial integration of the material acceleration (Wang, Zhang & Katz 2019). This integration uses a Graphics Processing Unit (GPU)-based, parallel-line, omni-directional algorithm, in which the pressure at each point is calculated by averaging integrations along paths aligned uniformly in all directions. The viscous effect is also accounted for in the near-wall region during the integration, i.e. $\nabla p = -\rho(D\mathbf{u}/Dt) + \mu \nabla^2 \mathbf{u}$, where ρ and μ are the pressure field and the dynamic viscosity, respectively. Experimental errors are further reduced by assigning weights to each path that are inversely proportional to the curl of the material acceleration. After integrations, the spatially averaged pressure is set to zero, hence the pressure discussed in this paper is the deviation of instantaneous pressure from the spatially averaged value. The uncertainty analysis in Agarwal *et al.* (2021) shows that the r.m.s. errors for velocity and pressure are less than $0.1u_\tau$ (3%) and $0.7\rho u_\tau^2$ (10%) at $y^+ > 80$, respectively. At lower elevations, the velocity error increases to $\sim 6\%$ at $y^+ = 10$ and that of the pressure remains similar. Ensemble averaging further reduces the uncertainty by an order of magnitude.

To measure the deformation, following Zhang *et al.* (2015) and Zhang *et al.* (2017), the interferogram intensity can be expressed as $I(x, z, t) = C_1(x, z, t) + 2C_2(x, z, t) \cos[\varphi_0(x, z) + (2\pi \Delta n / \lambda_0)d(x, z, t)]$, where C_1 and C_2 are the sum of wave intensities and the product of their amplitudes, respectively. The stationary term, φ_0 , accounts for the unperturbed wavefront, and can be removed by subtracting the time-averaged phase. In the second term, which accounts for the deformation, Δn is the difference between the refractive indices of the coating and the liquid, λ_0 is the laser wavelength in air, and d is the deformation height. Temporal normalization and correlation-based filtering are used for enhancing the fringes and homogenizing their peaks. The phase is determined from the arccosines, followed by unwrapping and detrending. The r.m.s. and peak uncertainty (Zhang *et al.* 2015) in deformation are 11 and 20 nm, respectively. Consistent with Wang *et al.* (2020), the present peak deformation, d_{peak} , increases from $0.2\delta_v$ to $3.5\delta_v$ as Re_τ increases from 3300 to 8900. The corresponding r.m.s. values, d_{rms} , increase from 0.03 to $0.44\delta_v$.

3. Results

3.1. Surface wave characteristics and their correlations with flow parameters

Figures 1(b) and 1(c) show sample instantaneous snapshots of the surface shape along with the pressure distribution in (x, y) planes coinciding with the deformation peaks at $Re_\tau = 3300$ and 6700, respectively. Corresponding movies are provided as supplementary movies 1 and 2 and are available at <https://doi.org/10.1017/jfm.2024.11>. Note that the deformation amplitude is exaggerated in comparison with the boundary-layer scales. As expected, a pressure minimum is located above a positive deformation ('bump'), and a maximum above a negative one ('dimple'). At all Re_τ , these pressure structures travel with the deformation peaks and appear to be phase locked with them, extending to well over $y^+ = 500$, even when the deformation amplitude is very small ($\sim 0.1\delta_v$ in figure 1b). Figure 2 presents streamwise wavenumber–frequency ($k_x - \omega$) spectra of the compliant

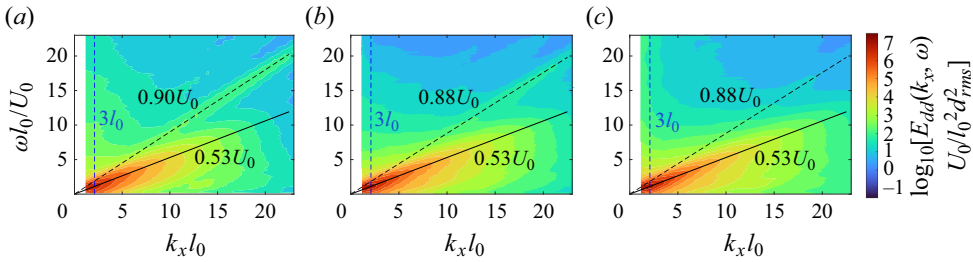


Figure 2. Streamwise wavenumber–frequency spectra of surface deformation for the following Re_τ and $E/(\rho U_0^2)$, respectively: (a) 3300,20.3; (b) 6700,4.5; and (c) 8900,2.5.

surface deformation at three Re_τ , where the wavenumber in rad/m is normalized by $1/l_0$ and the frequency in rad s^{-1} by U_0/l_0 , with l_0 being the compliant material thickness. The spectra are calculated using the 2-D fast Fourier transform function in Matlab[®] based on the entire database for each streamwise line, and then averaged in the spanwise direction. While the spectral peaks are located near the edge of the present wavenumber range, they correspond to a wavelength of $3l_0$, i.e. they do not vary with Re_τ , in agreement with the prediction of the Chase (1991) model and the experimental data by Wang *et al.* (2020). Yet, being centred around $\omega l_0/U_0 \sim 1.1$, the corresponding frequency increases with Re_τ . All the spectra contain a primary band indicating an advection speed of $U_{sw} = 0.53U_0$, and a secondary wave, which is 2 to 3 orders of magnitude weaker, that is advected at approximately $0.9U_0$. The latter is reported also in Zhang *et al.* (2017), but not in Wang *et al.* (2020), and owing to its small amplitude, the rest of the discussion focuses on the primary band. Prior studies of compliant wall boundary layers have reported advection speeds that scale with U_0 , with coefficients varying between 0.4 and 0.8, e.g. 0.40 in Kim & Choi (2014), 0.50 in Gad-el Hak (1986b), 0.53 in the present data, 0.65 in Esteghamatian *et al.* (2022), 0.66 in Wang *et al.* (2020), 0.70 in Dixon, Lucey & Carpenter (1994), 0.72 in Zhang *et al.* (2017) and 0.70–0.80 in Greidanus *et al.* (2022). Combining the entire data does not show persistent trends with material stiffness, density, thickness and Reynolds number. There are conflicts in the reported trends, e.g. measurements performed in our laboratory suggest an increase in U_{sw}/U_0 with increasing stiffness, while Greidanus *et al.* (2022) show a slight decrease. Trends with thickness also vary, with Kim & Choi (2014) and Gad-el Hak (1986b) reporting a decrease in speed with increasing thickness. Conversely, in Zhang *et al.* (2017) $U_{sw}/U_0 = 0.72$ for $l_0 = 16$ mm matches the Greidanus *et al.* (2022) values for $l_0 = 5$ mm, but not those of Wang *et al.* (2020) and the current data for the same thickness. Effects of density ratio and shear speed are also inconsistent. Even for the same set-up and material in our laboratory, the present value is lower than that in Wang *et al.* (2020). The only difference is the lower turbulence and large-scale fluctuations in the free-stream conditions. This unresolved topic is deferred to future studies, and might benefit from systematic numerical simulations.

The next discussion involves conditional statistics based on deformation magnitude, namely $d > \sigma_d$ for a bump and $d < -\sigma_d$ for a dimple (σ_d is the standard deviation), aimed at elucidating the relationship between deformation and the pressure, velocity and vorticity fields. Figures 3(a) and 3(b) show the planar surface pattern conditioned on a bump and a dimple, respectively. The spatial conditional correlations between flow variable $f(x, y, z, t)$ and $d(x, y, z, t)$ for a bump (for example) is defined as $\widetilde{C}_{f-d}(\Delta x, y, \Delta z)|_{d > \sigma_d} = \langle f(x_0 + \Delta x, y, z_0 + \Delta z, t)d(x_0, z_0, t) \rangle|_{d > \sigma_d} / [\sigma_f(x_0 + \Delta x, y, z_0 + \Delta z, t)\sigma_d(x_0, z_0, t)]|_{d > \sigma_d}$. These correlations are computed at 3552 points on

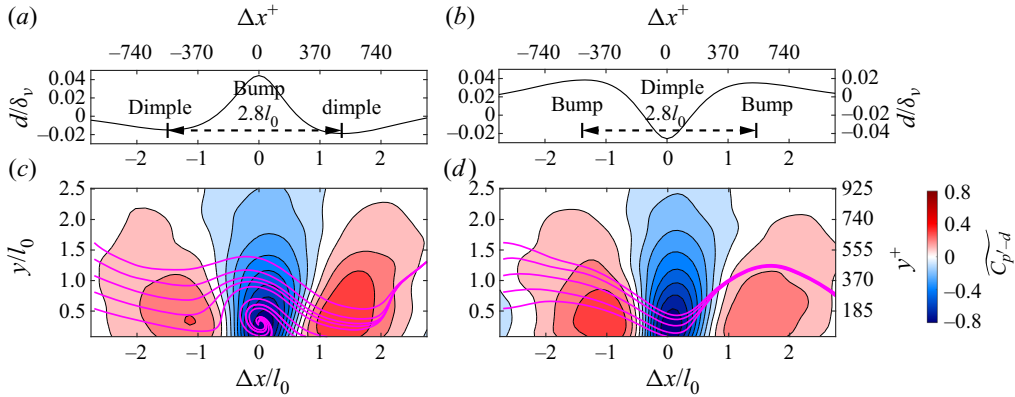


Figure 3. Conditional statistics for a surface bump (a,c) and a dimple (b,d), both for $Re_\tau = 3300$: (a,b) wall shape, and (c,d) p' - d correlation superimposed on conditional streamlines.

the compliant wall and then spatially and ensemble averaged. Results for $\widetilde{C}_{p'-d}$ at $Re_\tau = 3300$, which also include selected in-plane streamlines, are presented in figures 3(c) and 3(d) under the corresponding surface shapes. Maps of $\widetilde{C}_{u'-d}$, $\widetilde{C}_{v'-d}$, along with the conditionally averaged vertical vorticity, $\widetilde{\omega}_y^+$ and in-plane velocity vectors at $y^+ = 120$ are provided in supplementary figures S1(a–f). As is evident, the bump is bounded by dimples located on both sides and *vice versa*, and the characteristic wavelength is $2.8l_0$, close to $3l_0$, as predicted by the Chase (1991) model. The in-plane streamlines indicate that the bump is located under a spanwise vortex, and the dimple under the transition between ‘sweeping’ and ‘ejection’ events, downstream of the vortex. The velocity-deformation correlations peak in the sweeping flow region between the bump and the dimple, where the flow is induced, at least in part, by the vortex, but not necessarily in the same Δx . This vortex has a limited spanwise extent, approximately $400\delta_v$ (not shown), with lateral flow converging from both sides towards $\Delta z = 0$ (figure S1e). Once the sweeping flow impinges on the surface, the lateral flow diverges outward (figure S1f). The $\widetilde{\omega}_y^+$ maps show signatures of multiple counter-rotating, quasi-streamwise vortex pairs, with the peaks corresponding to a pair that generates a downward flow at $\Delta z = 0$ (opposite to a hairpin vortex). The $\widetilde{C}_{p'-d}$ peak for the bump is located slightly downstream of the spanwise vortex, at $\Delta x^+ = 30$, and $\Delta y^+ = 90$, and its magnitude, -0.8 (figure 3c), indicates that the pressure plays a primary role. There is also a slight shift of $\Delta x^+ = 30$ between the dimple and the location of minimum correlation at the sweep-ejection transition (figure 3d). Weaker positive peaks are located on both sides of the bump, corresponding to the high pressures above dimples, and *vice versa*. Above the bump, the pressure minimum is associated with both the spanwise vortex and the lateral acceleration, and above the dimple the pressure maximum is associated with lateral deceleration and inherent maximum at the sweep-ejection transition (Kim 1983). Before concluding this section, one should note that unlike the conditionally averaged flow field, many instantaneous realizations only contain fractions of the 3-D flow structures depicted in figure S1, e.g. an isolated spanwise vortex, or a quasi-streamwise vortex located on one of the sides of the bump.

The next point of discussion involves scaling the deformation height based on flow parameters and material properties, combining the present data with those of Zhang *et al.* (2017), Wang *et al.* (2020) and Greidanus *et al.* (2022). The materials used by Greidanus

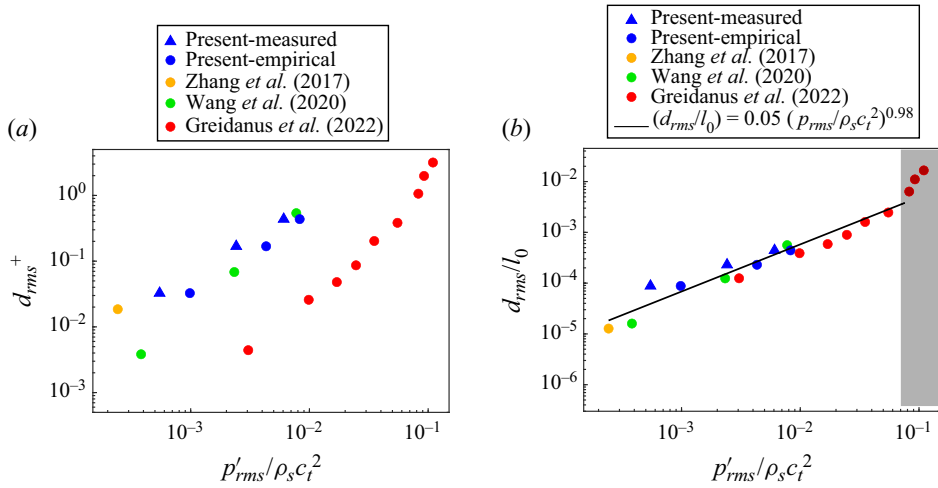


Figure 4. The r.m.s. of surface deformation scaled as (a) d_{rms}^+ , and (b) d_{rms}/l_0 plotted vs pressure fluctuations r.m.s. normalized by the shear modulus using data originated from several sources. The ‘Present-measured’ and Zhang *et al.* (2017) data for p'_{rms} are based on integration of material acceleration. The values for Greidanus *et al.* (2022), ‘Present-empirical’, and Wang *et al.* (2020) are estimated using Goody’s (2002) empirical model $(p'_{rms}/\rho u_\tau^2)^2 = 0.0309 + 0.745[\ln(u_\tau^2 \delta/U_0 \nu)]^2$.

et al. (2022) are softer than the present ones, and that used by Zhang *et al.* (2017) is an order of magnitude harder. Two methods are used to estimate the r.m.s. pressure: in Zhang *et al.* (2017) and for the present data, we integrate the material acceleration; for the rest, following Benschop *et al.* (2019), the r.m.s. pressure is estimated using the empirical model introduced by Goody (2002), namely $(p'_{rms}/(\rho u_\tau^2))^2 = 0.0309 + 0.745[\ln(u_\tau^2 \delta/(U_0 \nu))]^2$. To assess the compatibility of these methods, the model prediction for the present data, labelled ‘Present-empirical’, is compared with the ‘Present-measured’ values. In figure 4(a), the pressure is normalized by $G = \rho_s c_t^2$, where G , ρ_s and c_t are the shear modulus, density and shear speed of the elastomer, respectively. When d_{rms} is normalized by δ_ν (d_{rms}^+), trends of Zhang *et al.* (2017), Wang *et al.* (2019), and the present data do not agree with those in Greidanus *et al.* (2022). While the measured pressure is lower than the modelled values by 1.3 to 1.8, they still follow similar trends, hence the discrepancy in d_{rms}^+ is not caused by Goody’s (2002) empirical pressure estimate. In contrast, if the same data are plotted with the deformation scaled by the wall thickness, following Benschop *et al.* (2019) and Greidanus *et al.* (2022), the results collapse, as demonstrated in figure 4(b). This agreement includes the Zhang *et al.* (2017) data that has a different thickness (16 mm). The least-square-fitted power relationship excludes the data points at $p'_{rms}/(\rho_s c_t^2) > 0.076$ (shaded region in figure 4b), which according to Greidanus *et al.* (2022), fall in the nonlinear response range, where unstable waves develop on the compliant surface. The resulting empirical relation, $d_{rms}/l_0 = 0.05(p'_{rms}/(\rho_s c_t^2))^{0.98}$, covers more than two orders of magnitude of $p'_{rms}/(\rho_s c_t^2)$ and three orders of magnitude of d_{rms}/l_0 . This nearly linear relationship is consistent with the theoretical model introduced in Benschop *et al.* (2019) and the data presented in Greidanus *et al.* (2022). Note that Greidanus *et al.* (2022) provides many more data points for the range of their results, but we only include a sample of them to maintain a similar weight to data obtained from other sources. Furthermore, the linear

relationship could be interpreted as the longitudinal strain $\sim d_{rms}/l_0$ being proportional to the stress divided by the storage modulus, given that $G = E/[2(1 + \eta)]$, with η being the Poisson ratio. For $\eta = 0.5$, the relationship becomes $d_{rms}/l_0 \sim 0.15(p'_{rms}/E)$. The only parameter related to the flow is p'_{rms} . It should be emphasized that the trends depicted in [figure 4\(b\)](#) are likely to change as the compliant wall thickness becomes very large, and consequently, the interactions with the rigid wall under it diminish. Indeed, the theoretical analysis of wall response to harmonic excitation by Benschop *et al.* (2019) shows that when the compliant material thickness is much larger than the excitation wavelength, the deformation height becomes independent of l_0 , hence d_{rms}/l_0 diminishes.

3.2. Critical layer and near-wall turbulence

The following discussion focuses on the effect of the critical layer, where $U(y) = U_{sw}$ on the structure of near-wall turbulence. The critical heights are provided in [table 1](#) and marked in [figure 5\(a\)](#), along with profiles of $U(y)$ obtained using sum-of-correlation (SOC) with 4×4 pixel interrogation windows and 2-D projection of the 3-D data. Owing to the vertical resolution of the data, $118 \mu\text{m}/\text{interrogation height}$, the present measurements do not resolve the inner part of the boundary layers. Consequently, we also add sample SOC data based on 2-D PIV from Wang *et al.* (2020) for $Re_\tau = 8600$ that has been recorded at the same set-up. [Figures 5\(b\)–5\(g\)](#) present $k_x - \omega$ auto spectra of pressure, E_{pp} , as well as vertical, E_{vv} , and horizontal, E_{uu} , velocity fluctuations at $Re_\tau = 3300$. The upper row provides results for $y < y_c$, and the lower row, for $y > y_c$, with the solid and dashed lines indicating U_{sw} and $U(y)$, respectively. As is evident, at $y < y_c$, the slopes of the advection bands in E_{pp} and E_{vv} are equal to U_{sw} , i.e. the turbulence is advected with the deformation instead of the local flow. In E_{uu} , the advection band is wide and seems to be scale-dependent, being closer to $U(y)$ at low k_x but tilting towards U_{sw} with increasing k_x . In contrast, at $y > y_c$, all the bands indicate advection at $U(y)$, suggesting diminishing interactions with the wall motion. Using least-square fits to the bands, the advection speeds of p' , v' and u' as a function of y/y_c are plotted and compared with $U(y)$ and U_{sw} in [figures 5\(h\)–5\(j\)](#). For all three Re_τ , the advection speeds of p' and v' are equal to U_{sw} over the entire $y/y_c < 1$ regions, changing to $U(y)$ at $y/y_c > 1$. The advection speeds of u' also follow $U(y)$ at $y/y_c > 1$ but fall between $U(y)$ and U_{sw} at $y/y_c < 1$. Furthermore, the vertical profiles of maximum $\widetilde{C_{p'-d}}$, plotted in [figure 5\(k\)](#), indicate that the peak pressure–deformation correlation occurs at or slightly higher than $y = y_c$. Revisiting Zhang *et al.* (2017) for a stiffer wall, they also observe a peak in $\widetilde{C_{p'-d}}$ slightly above $y = y_c$. The high correlation peaks, 0.7–0.8, suggest that the pressure and deformations are phase locked, consistent with the direct observations and with measured coherence spectra ([supplementary figure S2](#)). Note that the correlation peak in [figure 5\(k\)](#) is slightly higher than y_c , but the coherence peak in [figure S2](#) is located at y_c . Since the coherence is based on pressure–deformation cross-spectra, it only accounts for the part of the turbulence spectrum that is coherent with the wave. In contrast, the correlation includes, in addition to the coherent part, contributions from turbulence that is not coherent with the wave. As a result, the $p' - d$ correlation peaks at a higher elevation than that of the coherent part. Considering that for some of the cases, the amplitude of wall motion is an order of magnitude smaller than the wall unit, these findings are striking. For example, the wall-normal extent of the region where the turbulence (especially the pressure) is highly correlated and advected with the wave expands from $63\delta_v$ at the lowest Re_τ , when $d_{rms}^+ = 0.03$ ($d_{peak}^+ = 0.22$), to nearly $200\delta_v$, when $d_{rms}^+ = 0.44$ ($d_{rms}^+ = 3.46$).

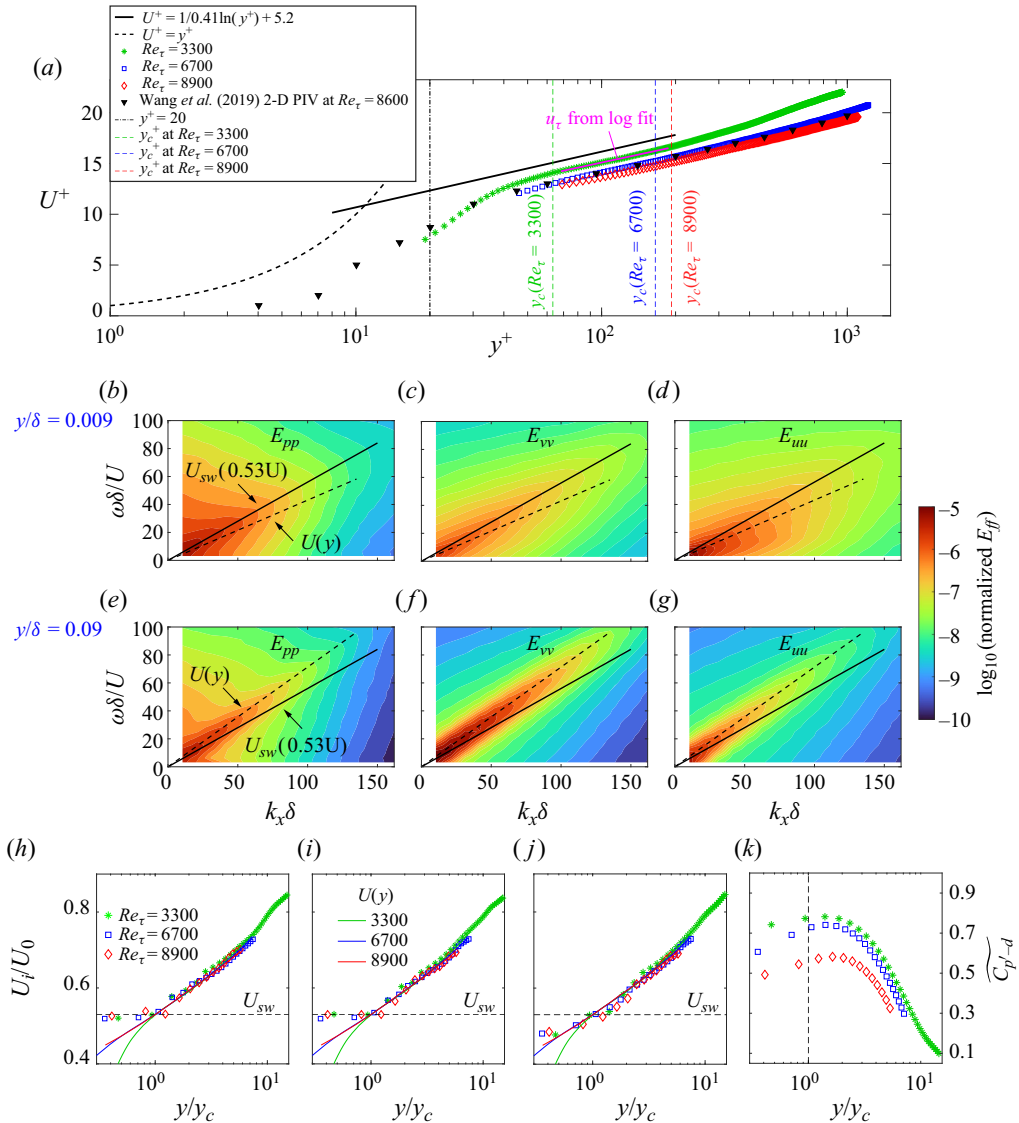


Figure 5. (a) Mean velocity profiles based on the present and 2-D PIV data of Wang *et al.* (2020), and corresponding critical heights in the present data. (b–g) Streamwise wavenumber–frequency spectra, E_{ff} , at $Re_\tau = 3300$: (b,e) $E_{pp}/[(\rho u_\tau^2 \delta)^2/U_0]$; (c,f) $E_{vv}/[(u_\tau \delta)^2/U_0]$; and (d,g) $E_{uu}/[(u_\tau \delta)^2/U_0]$. In (b–d) $y/\delta = 0.009$, i.e. $y < y_c$, and in (e–g) $y/\delta = 0.09$, i.e. $y > y_c$. (h–j) Profiles of advection speeds of (h) p' , (i) v' , (j) u' . Solid lines — $U(y)/U_0$; dashed lines $\cdots \cdots U_{sw}$. (k) Profiles of $p' - d$ correlation.

One may question whether the change in the near-wall advection speed is inherent to the inner part of turbulent boundary layers. Indeed, for channel flows over rigid smooth walls, DNS at $Re_\tau = 180$ (Kim & Hussain 1993), and experiments performed at $Re_\tau = 550$ (Schewe 1983) have shown that the advection speed at $y^+ \leq 20$ is equal to $U(y^+ = 20)$ for the pressure, and $U(y^+ = 15)$ for the velocity at $y^+ \leq 15$. Using the DNS data at $Re_\tau = 1000$ available in Johns Hopkins Turbulence Database (Graham *et al.* 2016), and obtaining the advection speed from the $k_x - \omega$ spectra, the trends agree with those of Kim & Hussain (1993), including the heights below which the advection speeds

are constant. Kim (1989) attributes these phenomena to the effect of quasi-streamwise vortices centred at $y^+ = 20$. In contrast, for the compliant wall, below the critical layer the wavelength and advection speed of pressure and vertical velocity events are equal to those of the compliant surface wave, with U_{sw} being significantly higher than $U(y^+ = 20)$. Furthermore, the turbulence and wave are phase locked and highly correlated even for $d_{rms}^+ \ll 1$. The height of this layer increases with increasing Re_τ extending deep into the log layer. Interestingly, y_c^+ is prescribed predominantly by the surface wave speed and would be nearly constant if not for modifications to the velocity profile caused by the deformation. In fact, as demonstrated in table 1, while y_c^+ increases significantly with Re_τ , when y_c is scaled with the boundary-layer thickness, y_c/δ fluctuates slightly and non-monotonically between 0.019 and 0.025. Since both y_c/δ and U_{sw}/U_0 are nearly constant, both appear to be related to outer layer parameters, and the expansion of the zone with strong turbulence-deformation coupling is associated with the downward shift of the mean velocity profile in the log layer.

3.3. Wall stress and mean velocity profile

An important question remains about whether the increase of friction drag, as indicated from the downward shift of the mean velocity profile, can be related to the surface ‘roughness’. Wang *et al.* (2020) provide direct comparisons between velocity profiles for a smooth rigid wall and a compliant wall at the same conditions (location in the tunnel, speed, tripping, etc.). The results show that for the entire range of Reynolds numbers, the compliant wall increases the wall shear stress by an amount that increases with deformation height. The significant drag increase, in spite of the small deformation amplitude, is most likely associated with dynamic interactions between the compliant wall and the flow, which affect both the form drag and the Reynolds stress at the wall. Hence the impact of the compliant wall should not be viewed as a roughness effect. As the shape of the wall changes, the pressure drag fluctuates spatially and temporally, and have alternate signs on the windward and leeward sides of the surface wave. Based on DNS data, Esteghamatian *et al.* (2022) show the net effect is an increase in drag. Furthermore, the wall motion forces the flow vertically through the $\langle p'v' \rangle$ correlations. Also, because of the wall motion, the Reynold shear stress does not diminish at the wall. Since the wave speed is higher than the flow speed below the critical layer, the Reynolds shear stress is likely to be negative, as confirmed in the DNS by Rosti & Brandt (2017) and Esteghamatian *et al.* (2022). Unfortunately, the spatial resolution of our measurements is insufficient for evaluating the pressure–velocity correlations, and the non-zero shear stress at the wall.

Before concluding, it would be of interest to examine the possible connection between the critical layer height and the Reynold stress profiles in the boundary layer. Morrill-Winter, Philip & Klewicki (2017) report that for a smooth rigid-wall boundary layer, the elevation of the Reynolds shear stress peak is $y_m^+ \sim 2\sqrt{\delta^+}$. While we do not include Reynolds stress profiles in the present paper (since the focus is scaling of the compliant wall response and impact of the critical layer on the deformation–turbulence interactions), the elevations of peak $\langle -u'v' \rangle$ are $y_m^+/\sqrt{\delta^+} = 2.00, 2.03$ and 2.04 at $Re_\tau = 3300, 6700$ and 8900 , respectively, i.e. they are very close to the smooth wall values. Furthermore, for two of the present cases, $Re_\tau = 6700$ and 8900 , the critical layer height is also located at the same elevation. However, at $Re_\tau = 3300$, $y_c^+ = 1.1\sqrt{(\delta^+)}$, i.e. well below y_m^+ . Similarly, y_c^+ is lower than y_m^+ for channel flow data presented in Zhang *et al.* (2017), and in the boundary layer results of Greidanus *et al.* (2022), with the latter being

inferred from the velocity profile and surface wave speed. Hence, y_c^+ is not necessarily associated with the peak in Reynolds stress.

4. Conclusions

Simultaneous measurements of the 3-D flow, pressure field, and wall deformation in a compliant wall boundary layer enable characterization of the coupling between the flow and surface motion. Conditional analysis reveals that the deformations are highly correlated with pressure fluctuations in the lower part of the log layer. The preferred wave speed of the deformation for all Re_τ , $0.53U_0$, falls within those of the previous reports that do not show clear trends with material properties or other parameters, a topic requiring further investigation. Combining data obtained from several references, trends of the deformation r.m.s. scaled by the compliant wall thickness collapse when plotted vs pressure fluctuations scaled by the compliant material shear modulus. The nearly linear relationship indicates that the longitudinal strain r.m.s. is proportional to the r.m.s. pressure scaled by the shear (or storage) modulus. To elucidate the impact of deformation wave on the flow field, we adopt the concept of a critical layer that has been developed for characterizing atmospheric wind–wave interactions. In the present data, the critical layer is located within the log layer, increasing in elevation with increasing Reynolds number. The pressure–deformation correlations peak, with magnitudes as high as 0.8, at or slightly above the critical layer. This observation is consistent with Lighthill's (1962) claim that most of the energy exchange between the flow and the wave occurs at the critical layer. At lower elevation, the turbulence is phase locked and travels with the surface wave even for deformation amplitudes much smaller than a wall unit. Above this layer, the turbulence is advected at the local mean streamwise velocity, and its correlation with the deformation decays rapidly. Hence, width of the zone with primary wall–turbulence interactions is predominantly prescribed by the surface wave speed. While the deformation height affects the magnitude of energy exchange with the flow, it only impacts the critical layer height through changes to the mean velocity profile.

Supplementary material and movies. Supplementary material and movies are available at <https://doi.org/10.1017/jfm.2024.11>.

Acknowledgements. The authors would like to dedicate this work to the late Y. Ronzhes, who designed the water tunnel.

Funding. This study is funded by the Office of Naval Research under grant numbers N00014-19-1-2096, N00014-23-1-2681 and N00014-20-1-2778. G. Orris is the program officer.

Declaration of interests. The authors report no conflict of interest.

Author ORCIDs.

📧 Tamer A. Zaki <https://orcid.org/0000-0002-1979-7748>;

📧 Joseph Katz <https://orcid.org/0000-0001-9067-2473>.

REFERENCES

- AGARWAL, K., RAM, O., WANG, J., LU, Y. & KATZ, J. 2021 Reconstructing velocity and pressure from noisy sparse particle tracks using constrained cost minimization. *Exp. Fluids* **62**, 1–20.
- BENSCHOP, H.O.G., GREIDANUS, A.J., DELFOS, R., WESTERWEEL, J. & BREUGEM, W.-P. 2019 Deformation of a linear viscoelastic compliant coating in a turbulent flow. *J. Fluid Mech.* **859**, 613–658.
- CARPENTER, J.R., BUCKLEY, M.P. & VERON, F. 2022 Evidence of the critical layer mechanism in growing wind waves. *J. Fluid Mech.* **948**, A26.

Scaling and critical layer in compliant wall boundary layers

- CARPENTER, J.R., GUHA, A. & HEIFETZ, E. 2017 A physical interpretation of the wind-wave instability as interacting waves. *J. Phys. Oceanogr.* **47** (6), 1441–1455.
- CARPENTER, P.W., DAVIES, C. & LUCEY, A.D. 2000 Hydrodynamics and compliant walls: does the dolphin have a secret? *J. Curr. Sci.* **79** (6), 758–765.
- CHASE, D.M. 1991 Generation of fluctuating normal stress in a viscoelastic layer by surface shear stress and pressure as in turbulent boundary-layer flow. *J. Acoust. Soc. Am.* **89** (6), 2589–2596.
- DIXON, A.E., LUCEY, A.D. & CARPENTER, P.W. 1994 Optimization of viscoelastic compliant walls for transition delay. *AIAA J.* **32** (2), 256–267.
- ESTEGHAMATIAN, A., KATZ, J. & ZAKI, T.A. 2022 Spatiotemporal characterization of turbulent channel flow with a hyperelastic compliant wall. *J. Fluid Mech.* **942**, A35.
- GAD-EL HAK, M. 1986a Boundary layer interactions with compliant coatings: an overview. *Trans. ASME J. Appl. Mech.* **39** (4), 411–524.
- GAD-EL HAK, M. 1986b The response of elastic and viscoelastic surfaces to a turbulent boundary layer. *Trans. ASME J. Appl. Mech.* **53**, 206–212.
- GOODY, M. 2002 An empirical spectral model of surface-pressure fluctuations that includes Reynolds number effects. In *8th AIAA/CEAS Aeroacoustics Conference & Exhibit*, p. 2565. AIAA.
- GRAHAM, J., *et al.* 2016 A web services accessible database of turbulent channel flow and its use for testing a new integral wall model for LES. *J. Turbul.* **17** (2), 181–215.
- GREIDANUS, A.J., DELFOS, R., PICKEN, S.J. & WESTERWEEL, J. 2022 Response regimes in the fluid–structure interaction of wall turbulence over a compliant coating. *J. Fluid Mech.* **952**, A1.
- KIM, E. & CHOI, H. 2014 Space–time characteristics of a compliant wall in a turbulent channel flow. *J. Fluid Mech.* **756**, 30–53.
- KIM, J. 1983 On the structure of wall-bounded turbulent flows. *Phys. Fluids* **26** (8), 2088–2097.
- KIM, J. 1989 On the structure of pressure fluctuations in simulated turbulent channel flow. *J. Fluid Mech.* **205**, 421–451.
- KIM, J. & HUSSAIN, F. 1993 Propagation velocity of perturbations in turbulent channel flow. *Phys. Fluids* **5** (3), 695–706.
- KRAMER, M.O. 1960 Boundary-layer stabilization by distributed damping. *J. Aerosp. Sci.* **27** (1), 69–69.
- LIGHTHILL, M.J. 1962 Physical interpretation of the mathematical theory of wave generation by wind. *J. Fluid Mech.* **14** (3), 385–398.
- MILES, J.W. 1957 On the generation of surface waves by shear flows. *J. Fluid Mech.* **3** (2), 185–204.
- MORRILL-WINTER, C., PHILIP, J. & KLEWICKI, J. 2017 An invariant representation of mean inertia: theoretical basis for a log law in turbulent boundary layers. *J. Fluid Mech.* **813**, 594–617.
- ROSTI, M.E. & BRANDT, L. 2017 Numerical simulation of turbulent channel flow over a viscous hyper-elastic wall. *J. Fluid Mech.* **830**, 708–735.
- SCHEWE, G. 1983 On the structure and resolution of wall-pressure fluctuations associated with turbulent boundary-layer flow. *J. Fluid Mech.* **134**, 311–328.
- WANG, J., KOLEY, S.S. & KATZ, J. 2020 On the interaction of a compliant wall with a turbulent boundary layer. *J. Fluid Mech.* **899**, A20.
- WANG, J., ZHANG, C. & KATZ, J. 2019 GPU-based, parallel-line, omni-directional integration of measured pressure gradient field to obtain the 3D pressure distribution. *Exp. Fluids* **60**, 1–24.
- YOUNG, W.R. & WOLFE, C.L. 2014 Generation of surface waves by shear-flow instability. *J. Fluid Mech.* **739**, 276–307.
- ZHANG, C., MIORINI, R. & KATZ, J. 2015 Integrating Mach–Zehnder Interferometry with TPIV to measure the time-resolved deformation of a compliant wall along with the 3D velocity field in a turbulent channel flow. *Exp. Fluids* **56**, 1–22.
- ZHANG, C., WANG, J., BLAKE, W. & KATZ, J. 2017 Deformation of a compliant wall in a turbulent channel flow. *J. Fluid Mech.* **823**, 345–390.